

On the intensity of focused waves near turning points

N. A. Lopez,^{1,2} E. Kur,³ and D. J. Strozzi³

¹*Department of Astrophysical Sciences, Princeton University, Princeton, New Jersey 08544, USA*

²*Rudolf Peierls Centre for Theoretical Physics, University of Oxford, Oxford OX1 3PU, UK*

³*Lawrence Livermore National Laboratory, Livermore, California 94551, USA*

A wave near an isolated turning point is typically assumed to have an Airy function profile with respect to the separation distance. This description is incomplete, however, and is insufficient to describe the behavior of more realistic wavefields that are not simple plane waves. Asymptotic matching to a prescribed incoming wavefield generically introduces a phasefront curvature term that changes the characteristic wave behavior from the Airy function to that of the hyperbolic umbilic function. This function, which is one of the seven classic ‘elementary’ functions from catastrophe theory along with the Airy function, can be understood intuitively as the solution for a linearly focused Gaussian beam propagating in a linearly varying density profile, as we show. The morphology of the caustic lines that govern the intensity maxima of the diffraction pattern as one alters the density lengthscale of the plasma, the focal length of the incident beam, and also the injection angle of the incident beam are presented in detail. This morphology includes a Goos-Hänchen shift and focal shift at oblique incidence that do not appear in a reduced ray-based description of the caustic. The enhancement of the intensity swelling factor for a focused wave compared to the typical Airy solution is highlighted, and the impact of finite lens aperture is discussed. Collisional damping and finite beam waist are included in the model and appear as complex components to the arguments of the hyperbolic umbilic function. The observations presented here on the behavior of waves near turning points should aid the development of improved reduced wave models to be used, for example, in designing modern nuclear fusion experiments.

I. INTRODUCTION

Basic wave physics is central to the development of controlled thermonuclear fusion. Indeed, a key component to the fusion milestones recently obtained at the National Ignition Facility (NIF)^{1,2} was leveraging the basic nonlinear optical process of cross-beam energy transfer (CBET) to maintain drive symmetry^{3,4}. That said, there still remain open questions regarding waves in fusion-relevant plasmas. One such question is the amount of reflection losses (i.e., glint) of an incident laser beam off the ablating hohlraum wall, an issue that was the focus of a recent experimental campaign on NIF⁵ for its possible connection to explaining the drive-deficit problem⁶. Being able to predict glint is paramount to future experimental performance because at sufficiently high intensities, the glint light may get nonlinearly amplified via CBET with lasers incident from the opposite entrance hole⁷ or even with light from the original laser^{8,9} to increase the amount lost. Moreover, researchers have recently begun to wonder¹⁰ whether the reflection physics might be modified by the speckle hot spots that are necessarily introduced to the NIF laser by the smoothing phase plates¹¹, since these are not currently accounted for in many inline laser modules. Hence, understanding the intensity profile of general wavefields near turning points has a renewed importance in fusion research.

For a plane wave incident on an isolated turning point (or turning plane in multiple dimensions), the intensity profile is well-known to be given by Airy’s function¹². For nonplanar wavefields, one can sometimes perform an asymptotic matching onto the Airy function and its derivative^{12,13}, but this can often obscure some of the key

properties of the true solution. Indeed, the Airy function is merely the simplest member of a large hierarchy of functions (the so-called diffraction integrals of catastrophe theory¹³⁻¹⁵) that can be used to describe wave behavior near critical points; since all members of this hierarchy contain the Airy function as a limiting behavior, it stands to reason that more general behavior might be more accurately and compactly captured by using higher order catastrophe functions.

Here it is shown that the behavior of a general wavefield near an isolated turning point can be compactly expressed as an integral mapping whose kernel is the hyperbolic umbilic function. The integral mapping takes the form of a convolution at normal incidence. As anticipated, the hyperbolic umbilic function is a higher member of the catastrophe hierarchy that allows non-plane-wave behavior near turning points (specifically, phasefront curvature) to be concisely described. By itself, the hyperbolic umbilic function also describes the solution for a Gaussian focused beam incident on a turning point. Since this function is not common in plasma physics, considerable space is dedicated to describing the morphology of the hyperbolic umbilic function as parameters of the problem are altered. The effects of dissipation and finite aperture width are also discussed. Due to their general nature, the results presented here will have applications beyond laser fusion experiments; for example, they may be useful for magnetic fusion researchers attempting to heat overdense plasmas via mode-conversion methods¹⁶⁻¹⁹, or attempting to measure turbulent fluctuations via Doppler backscattering^{20,21}.

This paper is organized as follows. In Sec. II the basic problem is set up. In Sec. III the general solution for

an arbitrary incident wavefield is obtained, which can be considered the main result of this work. In Sec. IV the special cases of a plane wave and a focused Gaussian wave (with and without aperture) are studied in detail as a means of understanding the general result presented in the previous section. Lastly, in Sec. V the main results are summarized. Additional discussions are provided in appendices.

II. PROBLEM SETUP

Let us consider a beam propagating in two dimensions (2-D)²² in a plasma that varies only in one direction, which we take to be x , with y being the remaining spatial direction. Since we are interested in the wavefield behavior near a turning point, we adopt a linear approximation of the plasma dielectric function (see Fig. 1):

$$\epsilon(x \geq 0) = 1 - \frac{x}{L(1 + i\nu)}, \quad (1)$$

where L is a constant length scale and $\nu \geq 0$ is a constant dimensionless damping coefficient. (Note that all numerical plots will have $\nu = 0$.) Hence, $x = 0$ corresponds to the vacuum-plasma interface (although it can be made to correspond to a more general boundary condition by setting $\epsilon(0) = \epsilon_0 > 0$ rather than unity). Lastly, let us assume the beam oscillates monochromatically in time and the plasma profile is stationary. Hence, we can partition the total wavefield \mathbf{E} as

$$\mathbf{E}(x, y, t) = \psi(x, y) \exp\left(-2\pi i \frac{ct}{\lambda}\right) \hat{\mathbf{e}} + c.c., \quad (2)$$

where c is the speed of light in vacuum, λ is the vacuum wavelength of the launched beam, and $\hat{\mathbf{e}}$ is the polarization vector. We shall further take \mathbf{E} to be s -polarized such that $\hat{\mathbf{e}}$ plays no role in the propagation dynamics and can be discarded.

III. GENERAL SOLUTION

A. Local solution near the turning point

Near the turning point for $x \geq 0$, the wavefield satisfies the Helmholtz equation

$$\left(\partial_x^2 + \partial_y^2 + \frac{L_c - x}{\delta_a^3}\right) \psi(x, y) = 0, \quad (3)$$

where we have introduced the complex lengthscale

$$L_c \doteq L(1 + i\nu), \quad (4)$$

along with the complex Airy skin depth

$$\delta_a \doteq \sqrt[3]{\frac{L_c \lambda^2}{4\pi^2}}. \quad (5)$$

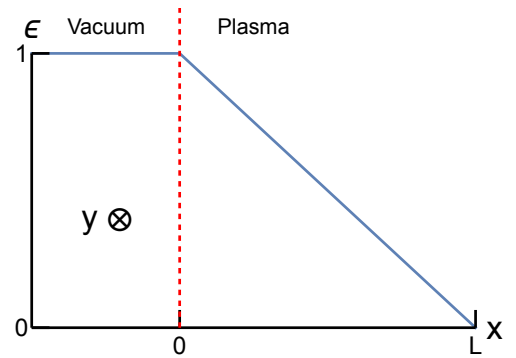


FIG. 1: The plasma dielectric function is assumed to be linear in x , with vacuum-plasma boundary at $x = 0$, and cutoff at $x = L$, and homogeneous in y , which, as noted, points into the page of the figure.

The conditions $L > 0$ and $\nu \geq 0$ restrict L_c to the first quadrant of the complex plane, i.e., $\arg(L_c) \in [0, \pi/2)$.

To proceed, let us apply a shifted Fourier transform (FT) in y . Our FT convention is as follows:²³

$$\tilde{f}(k_y) = \int \frac{dy}{\sqrt{2\pi}} f(y) \exp\left[-iy \left(k_y + \frac{2\pi}{\lambda} \sin \theta\right)\right], \quad (6a)$$

$$f(y) = \int \frac{dk_y}{\sqrt{2\pi}} \tilde{f}(k_y) \exp\left[iy \left(k_y + \frac{2\pi}{\lambda} \sin \theta\right)\right], \quad (6b)$$

where we have transformed out the mean wavevector $2\pi \sin \theta / \lambda$, which is assumed to be the predominant direction of k_y for oblique propagation. Applying Eq. (6) to Eq. (3) then yields

$$\left[\delta_a^2 \partial_x^2 - C \left(x, k_y + \frac{2\pi}{\lambda} \sin \theta\right)\right] \tilde{\psi}(x, k_y) = 0, \quad (7)$$

where we have introduced the cutoff function

$$C(x, k_y) \doteq \delta_a^2 k_y^2 + \frac{x - L_c}{\delta_a}. \quad (8)$$

Note that $\text{Re}(C) = 0$ defines the turning point for a plane wave propagating obliquely with transverse wavevector k_y . The solution to Eq. (7) which remains regular as $x \rightarrow +\infty$ is given by²⁴

$$\tilde{\psi}(x, k_y) = \frac{\text{Ai}\left[C \left(x, k_y + \frac{2\pi}{\lambda} \sin \theta\right)\right]}{\text{Ai}\left[C \left(0, k_y + \frac{2\pi}{\lambda} \sin \theta\right)\right]} \tilde{\psi}(0, k_y), \quad (9)$$

where Ai is the Airy function¹². The general solution for $x \geq 0$ can then be obtained by performing an inverse FT.

B. Asymptotic matching at plasma-vacuum boundary

Computing Eq. (9) requires knowing the total wavefield $\psi(0, y)$, which includes the interference between incoming and reflected components. This is difficult to construct when the reflected wavefield is itself the object of inquiry. An analogous equation to Eq. (9) that

depends only on the incoming field can be obtained via asymptotic matching as follows.

Suppose that the inverse-FT integral to obtain $\psi(x, y)$ from Eq. (9) is negligible beyond some characteristic maximum wavevector k_{\max} ²⁵. If the input plane $x = 0$ is located asymptotically far from the turning point for the maximum wavevector, i.e.,

$$-\operatorname{Re} \left[C \left(0, k_{\max} + \frac{2\pi}{\lambda} \sin \theta \right) \right] \gg 1, \quad (10)$$

then C at $x = 0$ is large and negative for all $|k_y| \leq k_{\max}$, and we can use the asymptotic approximation²⁶

$$\operatorname{Ai}[C(0)] \approx \frac{\cos \left\{ \frac{2}{3} [-C(0)]^{3/2} - \frac{\pi}{4} \right\}}{\sqrt{\pi} \sqrt[4]{-C(0)}}, \quad (11)$$

where here and in the following we have suppressed the second argument to C for brevity; it is understood to be $k_y + \frac{2\pi}{\lambda} \sin \theta$. Using Eq. (11) in Eq. (9) allows the incoming component to be isolated as

$$\tilde{\psi}_{\text{in}}(0, k_y) = \frac{\exp \left\{ -i \frac{2}{3} [-C(0)]^{3/2} \right\} \tilde{\psi}(x, k_y)}{\sqrt{-4\pi i} \sqrt[4]{-C(0)} \operatorname{Ai}[C(x)]}. \quad (12)$$

Note that the asymptotic matching condition (10) can also be understood as a paraxial requirement on the *incoming* field (but not necessarily the entire field), as anticipated by the shifted FT used in Eq. (6):

$$0 \leq k_{\max} \ll \frac{2\pi}{\lambda} \left(\sqrt{1 - \frac{\delta_a}{L}} - \sin \theta \right). \quad (13)$$

The necessary condition

$$\sin \theta \leq \sqrt{1 - \frac{\delta_a}{L}} \quad (14)$$

then places a limit on the maximum angle of incidence describable by our model. Physically, these two conditions (13) and (14) arise because oblique propagation

with transverse wavevector k_y shifts the turning point closer to the input plane by $\delta_a^3 k_y^2$, as seen from Eq. (8). Equations (14) and (13) therefore state that the turning points for the mean wavevector $2\pi \sin \theta / \lambda$ and for all deviations from the mean wavevector contained within the incoming wave spectrum are also located far from the input plane. Note also that for shallow incidence (θ large) when our matching scheme fails, one can instead perform the asymptotic matching spatially rather than spectrally because at such angles the overlap region between the incoming and reflected wavefields is small. At sufficiently shallow incidence, one might even be able to propagate ψ according to the paraxial wave equation, with the general solution for a linear density gradient provided in Ref. 27. We shall not pursue such generalizations here.

Further simplifications to Eq. (12) consistent with the paraxial approximation (13) can be performed²⁸. First, we make a slow-envelope approximation such that

$$\sqrt[4]{-C(0)} \approx \sqrt[6]{\frac{2\pi L_c}{\lambda} \cos^3 \theta}. \quad (15a)$$

However, we shall retain the k_y dependence in the phase:

$$[-C(0)]^{3/2} \approx \frac{2\pi L_c}{\lambda} \cos^3 \theta - \frac{3}{2} L_c k_y \sin 2\theta - \frac{3\lambda L_c k_y^2 \cos 2\theta}{4\pi \cos \theta}. \quad (15b)$$

Note that the approximations given by Eqs. (11) and (15) only alter the initial conditions of the Fourier-space solution (9) to the Helmholtz equation and hence preserve the ‘exactness’ of the solution. Said differently, the ψ obtained via Eq. (12) exactly solves Eq. (7) regardless the functional form of $C(0)$. These approximations instead alter which exact solution a given ψ_{in} is mapped to.

Performing an inverse FT to Eq. (12) and using Eqs. (15) therefore yields the matched solution

$$\psi(x, y) \approx \mathcal{N} \int dy' \psi_{\text{in}}(0, y') \mathcal{U}_{\text{H}} \left(\sqrt[3]{3} \frac{x - L_c}{\delta_a}, \frac{(y - y') \cos \theta - 2L_c \sin^3 \theta}{\sqrt[6]{3} \delta_a \cos \theta}, -\frac{\lambda L_c \cos 2\theta}{2\pi \sqrt[3]{3} \delta_a^2 \cos \theta} \right), \quad (16a)$$

or equivalently in terms of $\tilde{\psi}_{\text{in}}$ instead of ψ_{in} ,

$$\psi(x, y) \approx \mathcal{N} \sqrt{2\pi} \int du dv \tilde{\psi}_{\text{in}} \left(0, \frac{u}{\sqrt[6]{3} \delta_a} - \frac{2\pi}{\lambda} \sin \theta \right) \mathcal{U}_{\text{H}} \left(u, v, \sqrt[3]{3} \frac{x - L_c}{\delta_a}, \frac{y \cos \theta - 2L_c \sin^3 \theta}{\sqrt[6]{3} \delta_a \cos \theta}, -\frac{\lambda L_c \cos 2\theta}{2\pi \sqrt[3]{3} \delta_a^2 \cos \theta} \right), \quad (16b)$$

where the single integral over y' has been replaced by a double integral over u and v (which may in fact be easier to solve at times), the normalization constant is given as

$$\mathcal{N} \doteq \frac{\sqrt[6]{3}}{2\pi \sqrt{i\pi} \delta_a} \sqrt[6]{\frac{2\pi L_c}{\lambda} \cos^3 \theta} \exp \left(i \frac{4\pi L_c}{3\lambda} \frac{2 - \sin^2 \theta \cos 2\theta}{2 \cos \theta} \right), \quad (17)$$

and we have introduced the function U_H , defined as

$$U_H(t_1, t_2, t_3) \doteq \int du dv \mathcal{U}_H(u, v, t_1, t_2, t_3), \quad (18a)$$

and the function \mathcal{U}_H , defined as

$$\mathcal{U}_H(u, v, t_1, t_2, t_3) \doteq \exp(iu^2 v + iv^3 + it_3 u^2 + it_2 u + it_1 v), \quad (18b)$$

as the standard D_4^+ hyperbolic umbilic catastrophe function¹⁴ and the hyperbolic umbilic density function, respectively. U_H is one of the famous seven elementary diffraction catastrophes^{29,30} (the simplest of which being the Airy function). Note also that $[U_H(t_1, t_2, t_3)]^* = U_H(t_1, t_2, -t_3)$ and $U_H(t_1, -t_2, t_3) = U_H(t_1, t_2, t_3)$ when all parameters are real. We shall discuss U_H in more detail in the following section and in Appendix A.

Before doing so, however, it is worthwhile to emphasize the advantages of introducing U_H into the analysis. The main advantage is the structural stability of U_H . This feature both justifies the dropping of higher-order terms in Eq. (15b) by invoking strong 4-determinacy¹⁴ and suggests that the general phenomenon described by Eq. (16) will persist even if the problem setup changes moderately, i.e., replacing the linear plasma profile by an exponential profile more typical of a freely expanding plasma. As is apparent from Eq. (16), the structural stability of U_H also manifests as an ‘invariance’ of sorts with respect to injection angle: the injection angle appears simply as a parameter within the arguments of U_H that will cause the field profile to be translated, sheared, etc., but will not change the general functional behavior of the solution. [In fact, the angle-dependent terms in Eq. (16) can be identified as gradient-index analogues of the Goos–Hänchen and focal shifts³¹.] This is analogous to the ‘invariance’ of the Airy function (which is also structurally stable) to the injection angle as implied by Eq. (9). However, as we shall now show, the U_H representation is superior over the standard Airy representation due to its ability to compactly describe the fields that result from incident *beams* instead of plane waves.

IV. SPECIAL CASES

A. Special case: plane wave

As a sanity check, let us first confirm that Eq. (16) recovers the correct solution when ψ_{in} corresponds to a plane wave. Setting

$$\psi_{\text{in}}(0, y) = E_0 \exp\left(i \frac{2\pi y}{\lambda} \sin \theta\right) \quad (19)$$

(with E_0 a constant) in Eq. (16) yields

$$\begin{aligned} \psi(x, y) &= \frac{2\pi E_0}{\sqrt{i\pi}} \sqrt[6]{\frac{2\pi L_c}{\lambda} \cos^3 \theta} \text{Ai} \left[C \left(x, \frac{2\pi}{\lambda} \sin \theta \right) \right] \\ &\times \exp\left(i \frac{2\pi y}{\lambda} \sin \theta + i \frac{4\pi L_c}{3\lambda} \cos^3 \theta\right). \end{aligned} \quad (20)$$

as desired. (Note that the constants ensure the incoming component of Ai has amplitude E_0 .) Since $\max(\text{Ai}) \approx 0.5$ along the real line, one can estimate the swelling factor for the intensity of Eq. (20) when $\nu = 0$ as

$$\left| \frac{\psi_{\text{max}}}{\psi_{\text{in}}} \right|^2 \sim \left(\frac{2\pi L}{\lambda} \right)^{1/3} \pi \cos \theta, \quad (21)$$

which is in agreement with known results³². Importantly, the power-law scaling of the swelling factor (21) with respect to $1/\lambda$ (1/3) is equal to twice the singularity index of the fold catastrophe function^{12,15} (1/6), as expected.

B. Special case: focused Gaussian beam

To develop more intuition for what U_H is in Eq. (16), let us also consider the case when ψ_{in} corresponds to a focused wave with a Gaussian envelope:

$$\psi_{\text{in}}(0, y) = \frac{E_0 \cos \theta}{\sqrt{f_c/f}} \exp\left(i \frac{2\pi y}{\lambda} \sin \theta - i \frac{\pi y^2}{\lambda f_c} \cos^2 \theta\right), \quad (22)$$

which is the field behavior of a weakly focused Gaussian beam within a Rayleigh range of the focal plane³³. Here f_c is the complex beam parameter³³ (equivalently, a complex focal length) whose real and imaginary parts are $f_c \doteq f + i\varpi$, with f being the focal length and $\varpi \geq 0$ parameterizing the beam waist (with $\varpi = 0$ being a focused plane wave). Equation (16) then yields

$$\psi(x, y) = \bar{N} U_H \left(\sqrt[3]{3} \frac{x - L_c}{\delta_a}, \frac{y \cos \theta - 2L_c \sin^3 \theta - f_c \tan \theta}{\sqrt[6]{3} \delta_a \cos \theta}, \lambda \frac{f_c - 2L_c \cos 2\theta \cos \theta}{4\pi \sqrt[3]{3} \delta_a^2 \cos^2 \theta} \right), \quad (23)$$

where we have introduced the normalization constant

$$\bar{N} \doteq E_0 \frac{\sqrt[6]{3} \sqrt{\lambda f}}{2\pi i \sqrt{\pi} \delta_a} \sqrt[6]{\frac{2\pi L_c}{\lambda} \cos^3 \theta} \exp\left(i \frac{4\pi L_c}{3\lambda} \frac{2 - \sin^2 \theta \cos 2\theta}{2 \cos \theta} + i \frac{\pi f_c}{\lambda} \tan^2 \theta\right). \quad (24)$$

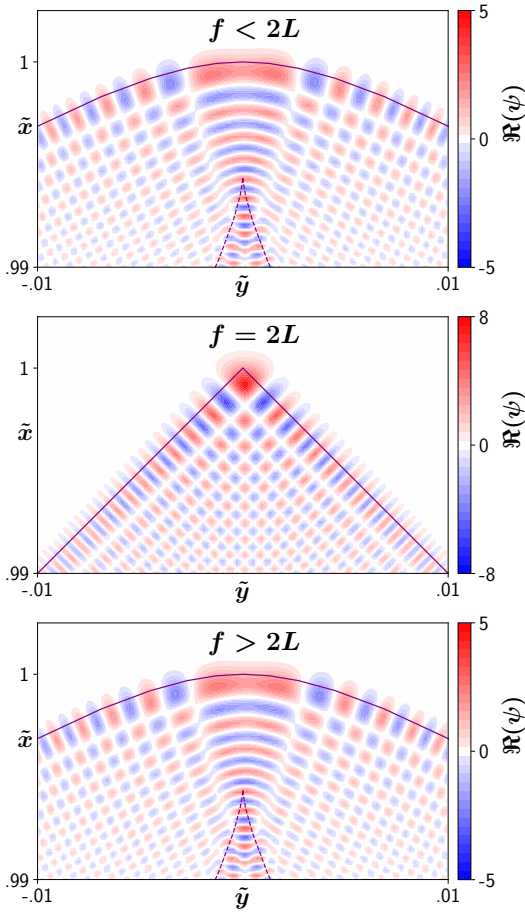


FIG. 2: The real part of the hyperbolic umbilic function, i.e., the solution (23) with $\bar{N} = 1$, $\nu = 0$, $\varpi = 0$, and $\theta = 0$ that describes a focused plane wave propagating in a linear plasma density profile at normal incidence. The purple lines mark the caustics given by Eqs. (26) or (27). For oblique incidence, the field pattern simply shifts laterally in y by the amount $2L \sin^2 \theta \tan \theta + f \tan \theta \sec \theta$, where the first term is the Goos–Hänchen shift and the second term corresponds to the shift in the launching point of the field component with transverse wavenumber equal to zero [Eq. (B4)]. Note that the spatial coordinates are normalized by L , and the distance between $\tilde{x} = 1$ and $\tilde{x} = 0.99$ constitutes 20 Airy skindepths, i.e., $L/\delta_a = 2000$.

Importantly, one should keep in mind that the paraxial condition (10) on the initial conditions requires that the complex focal length be sufficiently large:

$$|\tilde{f}_c| \gg \frac{2\pi}{\ell^{3/2}} \max \left[1, 4 \tan^2 \theta, \frac{\cos^2 \theta}{(\sqrt{1 - \ell^{-1}} - \sin \theta)^2} \right], \quad (25)$$

where $\ell \doteq L/\delta_a$ and $\tilde{f}_c \doteq f_c/L$. One also requires the necessary condition (14) to be satisfied. The solution (23) for $\bar{N} = 1$, $\nu = 0$, $\varpi = 0$, and $\theta = 0$ is shown in Fig. 2. (Choosing $\nu \neq 0$ and $\varpi \neq 0$ shifts the caustic into the complex domain; see Ref. 34 for a detailed discussion of the analogous phenomenon for the Airy function.)

Hence, we see that U_H can be intuitively understood as

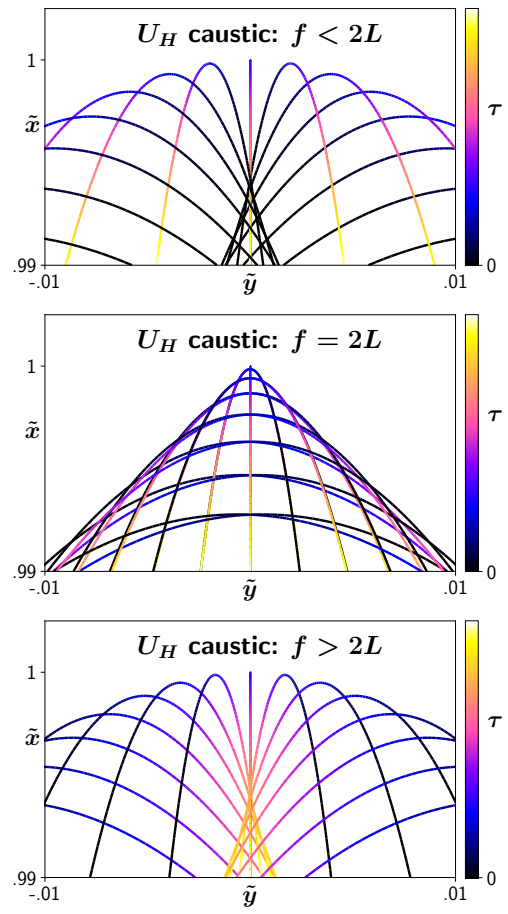


FIG. 3: Underlying ray trajectories (Appendix B) of the hyperbolic umbilic function shown in Fig. 2. Here, τ denotes the time along a ray: rays are launched at $\tau = 0$ and propagate with increasing τ . Hence, rays focus before reflecting off the critical density layer at $x = L$ when $f < 2L$, and focus after reflecting off the critical density layer when $f > 2L$. Moreover, the density gradient causes the focal spot to become aberrated as a cusp.

the field pattern that results when a focused plane wave of infinite extent encounters a simple turning point^{35,36}. This intuitive understanding is aided by considering a ray-based description of the wavefield propagation (Appendix B). Figure 3 shows ray trajectories that underlie U_H for three cases: (i) $f < 2L$, (ii) $f = 2L$, and (iii) $f > 2L$ at $\theta = 0$. Generally speaking, the focused rays enter the plasma and refract off the density profile according to their angle of incidence, which causes the focal point to become aberrated. When $f \neq 2L$, the rays either focus before reflecting off the high-density region or after, in accordance with the sign of $f - 2L$; for the special case of $f = 2L$ there is actually no aberrated focus, corresponding to the critical point of the hyperbolic umbilic function. The factor of two in the critical focal length is due to the enhanced gradient-index focusing³⁷ of the inhomogeneous plasma density profile - the incident beam must be focused nominally beyond the cutoff

to compensate. Also note that the ray equations are unable to describe the Goos-Hänchen and focal shifts that occur at finite θ , which is typical for such phenomena³⁸.

The caustic surfaces where local intensity maxima occur are given by Eqs. (A7)-(A9), which read in the normalized (x, y) variables (Appendix B) for the critical case $\tilde{f} = 2 \cos(2\theta) \cos \theta$ as

$$\tilde{x} \leq 1, \quad \tilde{y} = \sin(2\theta) \pm (\tilde{x} - 1), \quad (26)$$

and for the general case $\tilde{f} \neq 2 \cos(2\theta) \cos \theta$ by the parametric curves

$$\tilde{x}^{(\text{fold})} = 1 - \Delta \cosh(s) \frac{\cosh(s) - 1}{2}, \quad (27a)$$

$$\tilde{y}^{(\text{fold})} = \sin(2\theta) + 2\sqrt{\Delta} \sin \theta + \Delta \sinh(s) \frac{\cosh(s) + 1}{2}, \quad (27b)$$

$$\tilde{x}^{(\text{cusp})} = 1 - \Delta \cosh(s) \frac{\cosh(s) + 1}{2}, \quad (27c)$$

$$\tilde{y}^{(\text{fold})} = \sin(2\theta) + 2\sqrt{\Delta} \sin \theta + \Delta \sinh(s) \frac{\cosh(s) - 1}{2}, \quad (27d)$$

where $s \in (-\infty, \infty)$ is the curve parameterization and the fold-cusp separation distance Δ is given by

$$\Delta = \left[\frac{\tilde{f} - 2 \cos(2\theta) \cos \theta}{2 \cos^2 \theta} \right]^2. \quad (28)$$

We see the caustic of U_H typically consists of two parts: a parabolic-like fold line that constitutes the locus of turning points for the entire wavefield, and a semicubical-like cusp line that corresponds to a focal point aberrated by the plasma density gradient. The hyperbolic umbilic caustic stabilizes this fold-cusp network to perturbations in the problem setup, e.g., having a plasma density that deviates from the linear profile assumed here, or having a finite injection angle (the stability of which we have shown explicitly here).

When the incident wavefield is focused far from the critical density, the two caustic curves separate and the behavior near the turning point is well-described by an Airy function whose level sets are approximately parabolic [Eq. (A12)]. The intensity swelling factor would then be given by the usual formula (21). More generally, though, the two caustic curves influence each other to yield a field structure that is more sharply peaked than either the Airy or Pearcey function would predict alone^{12,14,15,36}. Indeed, since the peak value of U_H is approximately equal to 8 in the critically focused case (cf. Fig. 2), one can estimate the swelling factor for the intensity of Eq. (23) as

$$\left| \frac{\psi_{\text{max}}}{\psi_{\text{in}}} \right|^2 \sim 32f \sqrt[3]{\frac{12}{L\lambda^2\pi^4}} \cos \theta. \quad (29)$$

Again, the power-law scaling of the swelling factor (29) with respect to $1/\lambda$ (2/3) is equal to twice the singularity

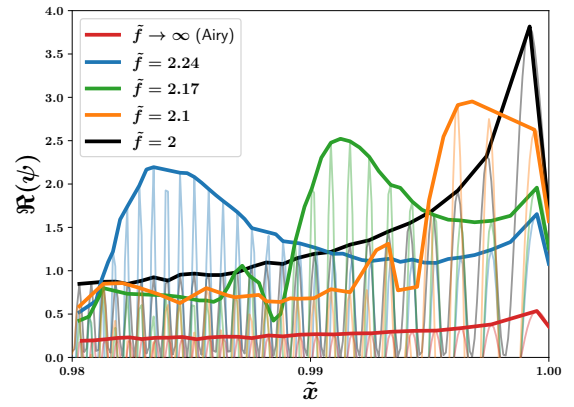


FIG. 4: Lineouts of the solution for ψ given by Eq. (23) along the symmetry axis $y = 0$ for various values of \tilde{f} . All cases have the same initial field amplitude at $\tilde{x} = 0$ given by $E_0 = \sqrt{i\pi} \exp(-i\frac{2}{3}\ell^{3/2})/2\pi\ell^{1/4}$; the visible differences in the field amplitude at $\tilde{x} = 0.98$ are due to the different swelling factors. The solid color lines shown the field envelope (given as the locus of all local maxima) for a given value of \tilde{f} , while the corresponding field oscillations are shown in a lighter shade. Clearly, the swelling of the field increases as the critical focusing condition $\tilde{f} = 2$ is approached. Note also that $\tilde{f} \rightarrow \infty$ recovers the standard Airy function solution (red), whose swelling factor is paltry in comparison.

index of the hyperbolic umbilic catastrophe function^{12,15} (1/3) by definition. The enhanced swelling of U_H compared to Ai is demonstrated in Fig. 4, which shows lineouts along the axis $y = 0$ for U_H at various values of \tilde{f} , including at $\tilde{f} \rightarrow \infty$ when U_H reduces to Ai [i.e., Eq. (23) reduces to Eq. (20)].

That said, however, the paraxial constraint (25) on the focal length means that one is not always able to realize the full morphology of U_H within our model, depending on the injection angle and the density lengthscale. A comparison between the critical focal length

$$\tilde{f}_{\text{crit}} = 2 \cos(2\theta) \cos \theta \quad (30)$$

that would create the most singular behavior of U_H and the minimum focal length set by Eq. (25) is shown in Fig. 5 for various values of ℓ . Immediately, one makes the curious observation that the critical focal length crosses zero at $\theta = \pi/4$ and becomes negative. This suggests that at large oblique angles the density gradient introduces such strong focal aberrations that one must launch a defocused (expanding) beam to obtain the critical behavior. Additionally, from the figure one sees that our model is only applicable over a small range of θ and \tilde{f} when the normalized density lengthscale is relatively short. As the lengthscale gets longer, the region of validity increases, although the zero crossing at $\theta = \pi/2$ always remains outside this region. (Note that for the NIF laser¹¹ with $\lambda = 351$ nm, the normalized lengthscales $\ell = 10, 100,$ and 1000 shown Fig. 5 correspond to absolute lengthscales of 0.002 mm, 0.05 mm, and 1.7 mm respectively.)

It is interesting to then consider how our model can

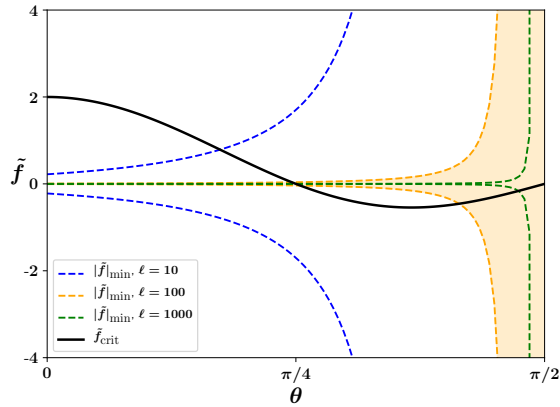


FIG. 5: Comparison for various values of the normalized density scale length ℓ between the critical focal length \tilde{f}_{crit} (black solid curve) and the minimum value \tilde{f}_{min} given by Eq. (25) that is required for the validity of Eq. (23). At a given ℓ , the critical focal length, and thus the most singular behavior of U_{H} (Fig. 2) with enhanced swelling given by Eq. (29), is only achievable for the range of obliquity angles θ for which the black line lies outside the region shaded by the respective color. Note that the focal length is normalized by the density scale length. For $\lambda = 351$ nm, the absolute lengthscales L shown in the plot are given respectively as 0.002 mm (blue), 0.05 mm (orange), and 1.7 mm (green).

be applied to present experiments. In particular, real experiments have a density profile that evolves in time. Consider the isothermal expansion of a laser-ablated hohlraum plasma for example. In such a plasma, the density lengthscale will increase as $L \sim C_s t$ with

$$C_s \doteq \sqrt{\frac{Z T_e}{m_i}} \quad (31)$$

being the sound speed, and correspondingly, our model's region of validity will steadily expand in time. Using the necessary condition (14) as means of a simple estimate, the NIF outer versus inner beams (which respectively make angles $\theta \sim 40^\circ$ and $\theta \sim 60^\circ$ with the hohlraum wall normal¹¹) can then be described after time $t \gtrsim 1.8$ ps and $t \gtrsim 6.4$ ps respectively. (Note that we have taken $T_e \sim 0.5$ keV, $Z \sim 20$, and $m_i = m_{\text{Au}}$ as typical early-time parameters for the ablating plasma.) This necessary delay time before our model can be applied to NIF-like parameters is negligible compared to the nanosecond timescales of the experiments. Furthermore, the steadily increasing Goos-Hänchen shift of the reflection point (equal to $2L \tan \theta \sin^2 \theta$) as time progresses suggests that ray-tracing calculations (which do not contain this shift) may become increasingly inaccurate at later times. This observation is particularly relevant be-

cause of the recent interest in characterizing glint losses in hohlraums⁵; if the reflection geometry is not specular but instead has angle-dependent shifts, the interpretation for which lasers are responsible for which glint signals may change (although the increased collisional absorption that also occurs at large L may dominate this effect in certain parameter regimes³⁹).

As the density evolves, the focusing of the incident wavefield will change even if the focal length of the lens remains the same. This is because increasing L drives \tilde{f} towards zero. A qualitative understanding of this effect can be readily obtained by viewing Fig. 5: when $\theta \leq \pi/4$ a wave with initial $\tilde{f} < 0$ will get more focused but never critically focused since it cannot cross $\tilde{f} = 0$, while a wave with $\tilde{f} > \tilde{f}_{\text{crit}}$ will become critically focused and then defocus; conversely, when $\theta > \pi/4$ a wave with $\tilde{f} \geq 0$ will become more focused but never critically focused, while a wave with $\tilde{f} < \tilde{f}_{\text{crit}}$ will pass through critically focusing on its way to becoming defocused. This generic behavior should be observable in other wave applications too, for example, electron cyclotron resonance heating on spherical tokamaks during the density rampup phase⁴⁰. Since ray-tracing codes are often used to optimize such applications, this observation means that advanced ray-tracing techniques such as etalon integrals^{8,34,41} or metaplectic geometrical optics^{27,42-44} are needed to enable the accurate computation of the entire unfolding of U_{H} .

C. Finite-aperture effects

Now let us consider how the presence of an aperture might modify the results thus far obtained. This is accomplished by letting⁴⁵

$$\psi_{\text{in}}(0, y) = \Psi_{\text{in}}(0, y) \text{rect}\left(\frac{y}{W}\right), \quad (32)$$

where $\text{rect}(z)$ denotes the rectangular hat function, which is everywhere zero except when $-1/2 < z < 1/2$ where it equals unity. The shifted FT of ψ is then given by the usual convolution formula

$$\tilde{\psi}_{\text{in}}(k_y) = \frac{W}{2\pi} \int d\kappa_y \text{sinc}\left(\frac{W\kappa_y}{2}\right) \tilde{\Psi}_{\text{in}}(k_y - \kappa_y). \quad (33)$$

In view of Eq. (16), if W is much larger than the characteristic variations in Ψ and U_{H} , then one can take $W \rightarrow \infty$ such that $\psi \approx \Psi$, meaning that the aperture plays no role. Similarly, if W is much smaller than the characteristic variations, one can take $W \rightarrow 0$ such that $\text{rect}\left(\frac{y}{W}\right) \approx W\delta(y)$ and one correspondingly obtains

$$\psi(x, y) \approx W \mathcal{N} \Psi_{\text{in}}(0, 0) U_{\text{H}} \left(\sqrt[3]{3} \frac{x - L_c}{\delta_a}, \frac{y \cos \theta - 2L_c \sin^3 \theta}{\sqrt[6]{3} \delta_a \cos \theta}, -\frac{\lambda L_c}{2\pi \sqrt[3]{3} \delta_a^2} \cos 2\theta \right), \quad (34)$$

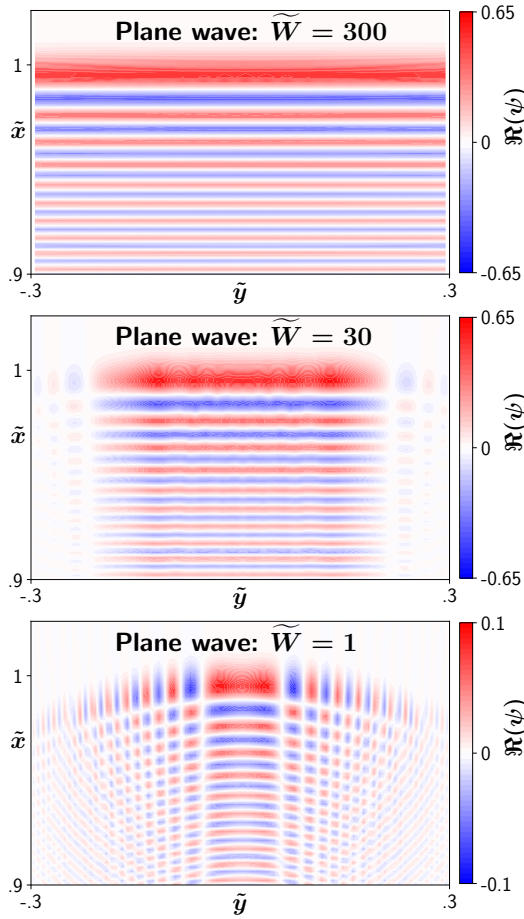


FIG. 6: Progression of the diffraction pattern for an apertured plane wave near a turning point located at $\tilde{x} = 1$ as the aperture width \tilde{W} is varied. The pattern transforms from the standard Airy pattern at large \tilde{W} to the defocused hyperbolic umbilic function (34) at small \tilde{W} according to Eq. (35), which is numerically solved using the method outlined in Appendix C. Here $L/\delta_a = 200$, so the distance between $\tilde{x} = 1$ and $\tilde{x} = 0.9$ constitutes 20 Airy skindepths.

where \mathcal{N} is given by Eq. (17). Hence, U_H can also be understood as the point-spread function⁴⁶ for propagation in a linear density gradient, since in this limit the signal that passes through the aperture can be considered a point source. Finite W will therefore generate a homotopic transformation between the unapertured solution (16) and the hyperbolic umbilic solution (34).

For an incident plane wave (Sec. IV A), the transformation is given explicitly as

$$\psi(x, y) \propto \frac{\sqrt[3]{3}\tilde{W}}{2\pi^2} \int du dv \operatorname{sinc}(\tilde{W}u) \times \mathcal{U}_H \left[u, v, \sqrt[3]{3}\ell(\tilde{x} - 1), \frac{\ell}{\sqrt[3]{3}}\tilde{y}, -\frac{\sqrt{\ell}}{\sqrt[3]{3}} \right], \quad (35)$$

where we have assumed $\theta = \nu = 0$ for simplicity. Also, we have re-introduced the normalized coordinates defined in

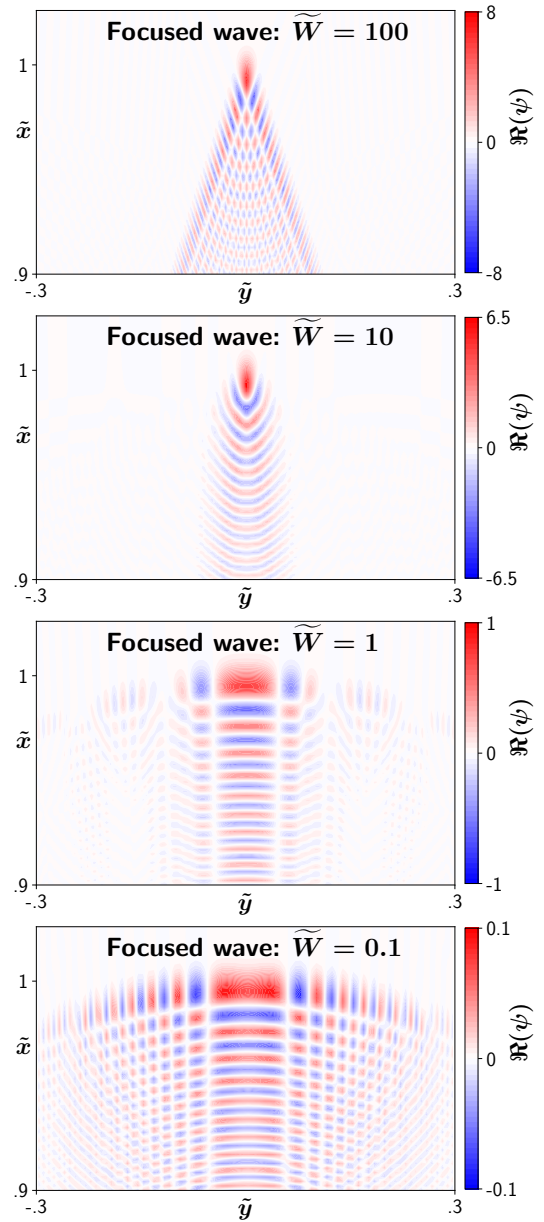


FIG. 7: Same as Fig. 6 but for the apertured focused wave described by Eq. (37) with critical focusing $\tilde{f} = 2$. The transitions for non-critical \tilde{f} are qualitatively similar.

Eqs. (B3) along with the normalized aperture width

$$\tilde{W} \doteq \frac{W}{2\sqrt[3]{3}\delta_a}. \quad (36)$$

One readily verifies that the hyperbolic umbilic solution (34) is recovered in the limit $\tilde{W} \rightarrow 0$ and the Airy solution (20) is recovered in the limit $\tilde{W} \rightarrow \infty$. This transition is shown in detail in Fig. 6, in which Eq. (35) is numerically calculated for various values of \tilde{W} .

Similarly, for an incident focused wave (Sec. IV B), the

transformation is given explicitly as

$$\psi(x, y) \propto \int du dv \frac{A(u)}{2} \times \mathcal{U}_H \left[u, v, \sqrt[3]{3}\ell(\tilde{x} - 1), \frac{\ell}{\sqrt[6]{3}}\tilde{y}, \frac{\sqrt{\ell}\tilde{f} - 2}{\sqrt[3]{3}} \right], \quad (37)$$

where we have taken $\theta = \nu = \varpi = 0$, and we have introduced the aperture function

$$A(u) \doteq \operatorname{erf} \left(\sqrt{\frac{i\tilde{f}}{2}} \frac{\sqrt[4]{\ell}}{\sqrt[6]{3}} u + \frac{\sqrt{i}\tilde{W}}{2} \right) - \operatorname{erf} \left(\sqrt{\frac{i\tilde{f}}{2}} \frac{\sqrt[4]{\ell}}{\sqrt[6]{3}} u - \frac{\sqrt{i}\tilde{W}}{2} \right). \quad (38)$$

For convenience, we have also altered our normalization convention for the aperture width such that now

$$\tilde{W} = \sqrt{\frac{\pi}{\lambda f}} W \quad (39)$$

(which one also recognizes as simply the Fresnel number of the aperture evaluated at the focal length⁴⁷). Again, one can verify that Eq. (34) is recovered from Eq. (37) in the limit $\tilde{W} \rightarrow 0$, and that Eq. (23) is obtained in the limit $\tilde{W} \rightarrow \infty$. The transformation between these two limiting cases is depicted in Fig. 7, where Eq. (37) is numerically computed for a sequence of \tilde{W} values.

V. CONCLUSIONS

In this work a model is proposed to describe the diffraction pattern of a general wavefield incident upon a turning point. Assuming that the incoming field has a bounded Fourier spectrum about the mean angle of incidence, the solution can then be expressed as an integral mapping of the initial wavefield whose kernel is the hyperbolic umbilic function, one of the seven famous functions from catastrophe theory. At normal incidence the integral takes the form of a convolution. It is shown that the traditional Airy solution is subsumed as a special case, and also that the hyperbolic umbilic function is itself a solution when the incident wavefield is Gaussian focused. Also, when the initial field is passed through an aperture, the solution generically transforms from the original aperture-free case to a defocused hyperbolic umbilic function, and explicit examples of this transformation are given for a plane wave and a Gaussian wave.

Due to the ubiquity of focused waves near turning points, the results presented here should have broad applications. In fusion research, these observations may enable the development of more accurate reduced models for lasers interacting with and reflecting off the hohlraum wall. It also lays the foundation for future studies to understand how the reflection physics might be modified

by the presence of speckles. Preliminary work¹⁰ suggests a speckled laser near a turning point can be described by a random sum of the apertured hyperbolic umbilic functions discussed here, although more analysis is required to confirm this finding and also to explore its consequences on modern ICF experiments. For certain phenomenological speckle models, e.g., treating speckled lasers as a sum of randomly focused Gaussian waves^{48–50}, these results may be immediately applicable.

ACKNOWLEDGMENTS

The authors thank P. Michel and T. Chapman for helpful conversations. This work was performed under the auspices of the U.S. Department of Energy by Lawrence Livermore National Laboratory under Contract DE-AC52-07NA27344.

DISCLOSURES

The authors declare no conflicts of interest.

Appendix A: Hyperbolic umbilic catastrophe function

The standard D_4^+ hyperbolic umbilic catastrophe function is defined in Ref. 14 as

$$U_H(t_1, t_2, t_3) \doteq \int du dv \exp(iu^2v + iv^3 + it_3u^2 + it_2u + it_1v). \quad (A1)$$

By making the variable substitution

$$u = \sqrt{3} \frac{\nu - \mu}{2^{2/3}}, \quad v = \frac{\nu + \mu}{2^{2/3}} - \frac{t_3}{2}, \quad (A2)$$

one can also transform U_H into the form

$$U_H(t_1, t_2, t_3) = \frac{\sqrt{3}}{\sqrt[3]{2}} \exp\left(-\frac{i}{2}t_1t_3 - \frac{i}{8}t_3^3\right) \tilde{U}_H\left(\frac{3t_3^2 + 4t_1 - 4\sqrt{3}t_2}{2^{8/3}}, \frac{3t_3^2 + 4t_1 + 4\sqrt{3}t_2}{2^{8/3}}, -\frac{3t_3}{\sqrt[3]{2}}\right), \quad (A3)$$

where \tilde{U}_H is the symmetrized hyperbolic umbilic catastrophe function used by Ref. 12:

$$\tilde{U}_H(\tau_1, \tau_2, \tau_3) \doteq \int d\nu d\mu \exp(i\nu^3 + i\mu^3 + i\tau_3\nu\mu + i\tau_2\nu + i\tau_1\mu). \quad (A4)$$

Additionally, the integration over v in Eq. (A1) can be explicitly performed to yield the representation

$$U_H(t_1, t_2, t_3) = \frac{2\pi}{\sqrt[3]{3}} \int du \operatorname{Ai}\left(\frac{u^2 + t_1}{\sqrt[3]{3}}\right) \times \exp(it_3u^2 + it_2u). \quad (A5)$$

Similarly, one can perform the Gaussian integration over u in Eq. (A1) and then make the variable transformation $z = \sqrt{v} + t_3$ to obtain the representation

$$U_H(t_1, t_2, t_3) = 2\sqrt{i\pi} \exp(-it_3^3 - it_1 t_3) \times \int_{i\infty}^{\infty} dz \exp \left[iz^6 - 3it_3 z^4 + i(3t_3^2 + t_1)z^2 - i\frac{t_2^2}{4z^2} \right], \quad (\text{A6})$$

where the integration contour passes from $+i\infty$ on the imaginary axis towards the origin, passing to the upper right of the essential singularity at $z = 0$, then continuing towards $+\infty$ on the real line. Equation (A5) is useful for numerical computation, as discussed further in Appendix C, while Eq. (A6) is useful for understanding the (nontrivial) asymptotic behavior of U_H via steepest-descent methods, as discussed further in Ref. 51.

Important for our purposes are the caustic surfaces of U_H . At fixed $t_3 \neq 0$, these caustics consist of one fold line and one cusp line in the $t_1 - t_2$ plane, given by the parametric equations

$$t_1^{(\text{fold})} = -\frac{3}{2}t_3^2 \cosh(s) [\cosh(s) - 1], \quad (\text{A7a})$$

$$t_2^{(\text{fold})} = \frac{\sqrt{3}}{2}t_3^2 \sinh(s) [\cosh(s) + 1], \quad (\text{A7b})$$

and

$$t_1^{(\text{cusp})} = -\frac{3}{2}t_3^2 \cosh(s) [\cosh(s) + 1], \quad (\text{A8a})$$

$$t_2^{(\text{cusp})} = \frac{\sqrt{3}}{2}t_3^2 \sinh(s) [\cosh(s) - 1], \quad (\text{A8b})$$

where the parameterization s ranges from $-\infty$ to ∞ . When $t_3 = 0$, the fold and cusp lines coalesce into the line segments

$$t_1 \leq 0, \quad t_2 = \frac{t_1}{\sqrt{3}}, \quad (\text{A9a})$$

$$t_1 \leq 0, \quad t_2 = -\frac{t_1}{\sqrt{3}}. \quad (\text{A9b})$$

For $t_2 \approx 0$ (equiv., $s \approx 0$) and $t_3 \neq 0$, the fold and cusp lines are approximately represented as

$$t_1^{(\text{fold})} \approx -\left(\frac{t_2}{2t_3}\right)^2, \quad (\text{A10a})$$

$$t_1^{(\text{cusp})} \approx -3t_3^2 - 9\left(\frac{t_2 t_3}{2\sqrt{3}}\right)^{2/3}. \quad (\text{A10b})$$

Hence, the characteristic fold-line width, cusp-line width, and fold-cusp separation are respectively t_3 , $1/t_3$, and t_3^2 .

Since the fold and cusp lines become increasingly separated as $|t_3|$ increases, one expects that in the asymptotic limit $|t_3| \rightarrow \infty$ the hyperbolic umbilic function can be approximately represented as an Airy function. Indeed, by

completing the square in Eq. (A5), one can represent U_H as

$$U_H(t_1, t_2, t_3) = \frac{2\pi}{\sqrt[3]{3}} \exp\left(-i\frac{t_2^2}{4t_3}\right) \int du \text{Ai}\left(\frac{u^2 + t_1}{\sqrt[3]{3}}\right) \times \exp\left[it_3\left(u + \frac{t_2}{2t_3}\right)^2\right]. \quad (\text{A11})$$

As $|t_3| \rightarrow \infty$, the integral will thus be dominated by the contributions around the stationary point $u = -t_2/(2t_3)$. Hence, standard stationary phase methods yield the approximation

$$U_H(t_1, t_2, t_3) \approx \frac{2\pi}{\sqrt[3]{3}} \sqrt{i\pi} \frac{1}{t_3} \text{Ai}\left[\frac{t_1 + (t_2/2t_3)^2}{\sqrt[3]{3}}\right] \times \exp\left(-i\frac{t_2^2}{4t_3}\right). \quad (\text{A12})$$

Note that the argument to the Airy function is simply the quadratic approximation to the fold line presented in Eq. (A10a); hence, the basic structure of Eq. (A12) can be anticipated from the principles of catastrophe optics.

Appendix B: Ray equations for visualizing the caustic skeleton of U_H

In the following, we neglect the dissipation and finite beamwaist terms such that all physical parameters are real. For the wave equation given in Eq. (3), the dispersion symbol⁵² that governs the propagation of the geometrical-optics rays is calculated to be

$$\mathcal{D}(x, y, k_x, k_y) = k_x^2 + k_y^2 + \frac{x - L}{\delta_a^3}. \quad (\text{B1})$$

The rays then satisfy the dynamical equations

$$\partial_\tau x(\tau) = 2k_x(\tau), \quad \partial_\tau k_x(\tau) = -\frac{1}{\delta_a^3}, \quad (\text{B2a})$$

$$\partial_\tau y(\tau) = 2k_y(\tau), \quad \partial_\tau k_y(\tau) = 0. \quad (\text{B2b})$$

Let us normalize all wavenumber-like quantities by the vacuum wavenumber $2\pi/\lambda$, all distance-like quantities by the density lengthscale L , and the ray propagation time (which has units of length squared) by their product:

$$\tilde{x} = \frac{x}{L}, \quad \tilde{y} = \frac{y}{L}, \quad \tilde{f} = \frac{f}{L}, \quad (\text{B3a})$$

$$\tilde{k}_x = \frac{\lambda k_x}{2\pi}, \quad \tilde{k}_y = \frac{\lambda k_y}{2\pi}, \quad \tilde{\tau} = \frac{2\pi\tau}{\lambda L}. \quad (\text{B3b})$$

Let us choose $\tilde{x}(0) = 0$ and $\tilde{y}(0) = \tilde{y}_0$. The initial condition (22) for U_H implies that the rays have the corresponding initial condition

$$\tilde{k}_y(0) = \sin \theta - \frac{\tilde{y}_0}{\tilde{f}} \cos^2 \theta. \quad (\text{B4})$$

The condition $\mathcal{D} = 0$ then determines the remaining initial condition:

$$\tilde{k}_x(0) = \sqrt{1 - \tilde{k}_y^2(0)}. \quad (\text{B5})$$

The normalized ray trajectories that satisfy Eq. (B2) subject to the initial conditions are then given as

$$\tilde{x}(\tilde{\tau}) = 2\tilde{k}_x(0)\tilde{\tau} - \tilde{\tau}^2, \quad \tilde{k}_x(\tilde{\tau}) = \tilde{k}_x(0) - \tilde{\tau}, \quad (\text{B6a})$$

$$\tilde{y}(\tilde{\tau}) = \tilde{y}_0 + 2\tilde{k}_y(0)\tilde{\tau}, \quad \tilde{k}_y(\tilde{\tau}) = \tilde{k}_y(0). \quad (\text{B6b})$$

Note that the ray equations (B6) only describe the hyperbolic umbilic caustic pattern close to the critical point due to us applying an asymptotic initial condition at a finite location. Aberrations manifest farther from the critical point that cause the ray envelope caustic to deviate from the true caustic, although some authors choose to accommodate such aberrations in their unfolding convention for U_H (equivalently, generically consider observations on curved surfaces rather than planes) to simplify the process of identifying this caustic in real experiments (see, for example, Figs. 4.4 and 4.5 in Ref. 53).

Appendix C: Numerical procedure for computing U_H and related functions

Here we provide a simple procedure for computing $U_H(t_1, t_2, t_3)$ and related integrals using the representation provided by Eq. (A5). First, when $t_3 = 0$ one can use results from Ref. 54 to obtain the exact expression

$$U_H(t_1, t_2, 0) = 2\pi^2 \sqrt[6]{\frac{16}{3}} \text{Ai}\left(\frac{t_1 - \sqrt{3}t_2}{\sqrt[3]{12}}\right) \times \text{Ai}\left(\frac{t_1 + \sqrt{3}t_2}{\sqrt[3]{12}}\right). \quad (\text{C1})$$

For general $t_3 \neq 0$, Eq. (A5) takes the form of an FT:

$$U_H(t_1, t_2, t_3) = \frac{2\pi}{\sqrt[3]{3}} \mathcal{F}_u \left[\text{Ai}\left(\frac{u^2 + t_1}{\sqrt[3]{3}}\right) \exp(it_3 u^2) \right] (t_2), \quad (\text{C2})$$

where $\mathcal{F}_u[f(u)](k)$ denotes the FT of $f(u)$, now considered a function of k defined as

$$\mathcal{F}_u[f(u)](k) \doteq \int du f(u) \exp(-iku). \quad (\text{C3})$$

Equation (C2) can then be computed using standard FFT routines, which is how Fig. 2 was produced.

The apertured formulas of Sec. IV C can be computed similarly. Equation (35) is computed via FFT as

$$\psi \propto \frac{\tilde{W}}{\pi} \mathcal{F}_u \left[\text{sinc}(\tilde{W}u) \text{Ai}\left(\frac{u^2 + t_1}{\sqrt[3]{3}}\right) \exp(it_3 u^2) \right] (t_2), \quad (\text{C4})$$

where t_1 , t_2 , and t_3 are the arguments for U_H in Eq. (35), while Eq. (37) is computed as

$$\psi \propto \frac{\pi}{\sqrt[3]{3}} \mathcal{F}_u \left[A(u) \text{Ai}\left(\frac{u^2 + t_1}{\sqrt[3]{3}}\right) \exp(it_3 u^2) \right] (t_2), \quad (\text{C5})$$

where t_1 , t_2 , and t_3 are the arguments for U_H in Eq. (37). Figures 6 and 7 are computed using these formulas.

- ¹H. Abu-Shawareb and others (Indirect Drive ICF Collaboration), *Phys. Rev. Lett.* **129**, 075001 (2022).
- ²A. B. Zylstra, O. A. Hurricane, D. A. Callahan, A. L. Kritcher, J. E. Ralph, H. F. Robey, J. S. Ross, C. V. Young, K. L. Baker, D. T. Casey, *et al.*, *Nature* **601**, 542 (2022).
- ³P. Michel, L. Divol, E. A. Williams, S. Weber, C. A. Thomas, D. A. Callahan, S. W. Haan, J. D. Salmonson, S. Dixit, D. E. Hinkel, M. J. Edwards, B. J. MacGowan, J. D. Lindl, S. H. Glenzer, and L. J. Suter, *Phys. Rev. Lett.* **102**, 025004 (2009).
- ⁴P. Michel, S. H. Glenzer, L. Divol, D. K. Bradley, D. Callahan, S. Dixit, S. Glenn, D. Hinkel, R. K. Kirkwood, J. L. Kline, W. L. Kruer, G. A. Kyrala, S. Le Pape, N. B. Meezan, R. Town, K. Widmann, E. A. Williams, B. J. MacGowan, J. Lindl, and L. J. Suter, *Phys. Plasmas* **17**, 056305 (2010).
- ⁵N. Lemos, W. A. Farmer, N. Izumi, H. Chen, E. Kur, A. Pak, B. B. Pollock, J. D. Moody, J. S. Ross, D. E. Hinkel, O. S. Jones, T. Chapman, N. B. Meezan, P. A. Michel, and O. L. Landen, *Phys. Plasmas* **29**, 092704 (2022).
- ⁶O. S. Jones, L. J. Suter, H. A. Scott, M. A. Barrios, W. A. Farmer, S. B. Hansen, D. A. Liedahl, C. W. Mauche, A. S. Moore, M. D. Rosen, J. D. Salmonson, D. J. Strozzi, C. A. Thomas, and D. P. Turnbull, *Phys. Plasmas* **24**, 056312 (2017).
- ⁷D. Turnbull, P. Michel, J. E. Ralph, L. Divol, J. S. Ross, L. F. B. Hopkins, A. L. Kritcher, D. E. Hinkel, and J. D. Moody, *Phys. Rev. Lett.* **114**, 125001 (2015).
- ⁸A. Colaitis, R. K. Follett, J. P. Palastro, I. Igumenshchev, and V. Goncharov, *Phys. Plasmas* **26**, 072706 (2019).
- ⁹E. Kur, J. Wurtele, and P. Michel, *Bull. Am. Phys. Soc.* **62**, Abstract NO06.010 (2020).
- ¹⁰N. A. Lopez, E. Kur, T. D. Chapman, D. J. Strozzi, and P. A. Michel, *Bull. Am. Phys. Soc.* **63**, Abstract NP11:00063 (2021).
- ¹¹M. L. Spaeth, K. R. Manes, D. G. Kalantar, P. E. Miller, J. E. Heebner, E. S. Bliss, D. R. Spec, T. G. Parham, P. K. Whitman, P. J. Wegner, P. A. Baisden, J. A. Menapace, M. W. Bowers, S. J. Cohen, T. I. Suratwala, J. M. Di Nicola, M. A. Newton, J. J. Adams, J. B. Trenholme, R. G. Finucane, R. E. Bonanno, D. C. Rardin, P. A. Arnold, S. N. Dixit, G. V. Erbert, A. C. Erlandson, J. E. Fair, E. Feigenbaum, W. H. Gourdin, R. A. Hawley, J. Honig, R. K. House, K. S. Jancaitis, K. N. LaFortune, D. W. Larson, B. J. Le Galloudec, J. D. Lindl, B. J. MacGowan, C. D. Marshall, K. P. McCandless, R. W. McCracken, R. C. Montesanti, E. I. Moses, M. C. Nostrand, J. A. Pryatel, V. S. Roberts, S. B. Rodrigues, A. W. Rowe, R. A. Sacks, J. T. Salmon, M. J. Shaw, S. Sommer, C. J. Stolz, G. L. Tietbohl, C. C. Widmayer, and R. Zacharias, *Fusion Sci. Technol.* **69**, 25 (2017).
- ¹²F. W. J. Olver, D. W. Lozier, R. F. Boisvert, and C. W. Clark, *NIST Handbook of Mathematical Functions* (Cambridge: Cambridge University Press, 2010).
- ¹³Y. A. Kravtsov and Y. I. Orlov, *Caustics, Catastrophes and Wave Fields* (Berlin: Springer, 1993).
- ¹⁴T. Poston and I. Stewart, *Catastrophe Theory and Its Applications* (New York: Dover, 1996).
- ¹⁵M. V. Berry and C. Upstill, *Prog. Opt.* **18**, 257 (1980).
- ¹⁶H. Igami, H. Tanaka, and T. Maekawa, *Plasma Phys. Control. Fusion* **48**, 573 (2006).
- ¹⁷J. Urban, J. Decker, Y. Peysson, J. Preinhaelter, V. Shevchenko, G. Taylor, L. Vahala, and G. Vahala, *Nucl. Fusion* **51**, 083050 (2011).
- ¹⁸G. Taylor, R. A. Ellis, E. Fredd, S. P. Gerhardt, N. Greenough, R. W. Harvey, J. C. Hosea, R. Parker, F. Poli, R. Raman, S. Shi-

- raiva, A. P. Smirnov, D. Terry, G. Wallace, and S. Wukitch, *EPJ Web of Conf.* **87**, 02013 (2015).
- ¹⁹N. A. Lopez and A. K. Ram, *Plasma Phys. Control. Fusion* **60**, 125012 (2018).
- ²⁰J. Ruiz Ruiz, F. I. Parra, V. H. Hall-Chen, N. Christen, M. Barnes, J. Candy, J. Garcia, C. Giroud, W. Guttenfelder, J. C. Hillesheim, C. Holland, N. T. Howard, Y. Ren, A. E. White, and JET contributors, *Plasma Phys. Control. Fusion* **64**, 055019 (2022).
- ²¹V. H. Hall-Chen, F. I. Parra, and J. C. Hillesheim, *Plasma Phys. Control. Fusion* **64**, 095002 (2022).
- ²²The following analysis can be readily generalized to arbitrary number of dimensions through only cosmetic modifications.
- ²³All integrals range from $-\infty$ to $+\infty$ unless explicitly stated.
- ²⁴The restriction $\arg(L_c) \in [0, \pi/2)$ in turn restricts $\arg(C) \in [0, -\pi/6)$ as $x \rightarrow +\infty$; hence, no Stokes' phenomenon correction to Eq. (9) are needed as these would require $|\arg(C)| \geq \pi/3$ ⁵⁵.
- ²⁵This might be either because for $|k_y| > k_{\max}$ the spectrum of ψ decays rapidly to zero or the integral itself becomes increasingly oscillatory and averages to zero.
- ²⁶Again, no Stokes' phenomenon corrections are needed because $\arg(-C) \approx \arg(L_c/\delta_a) \in [0, \pi/3)$ is within the wedge of validity $\arg(\zeta) \in (-2\pi/3, 2\pi/3)$ for the standard asymptotic expansion of $\text{Ai}(-\zeta)$ ¹².
- ²⁷N. A. Lopez, *Metaplectic geometrical optics*, Ph.D. thesis, Princeton University (2022).
- ²⁸Formally, Eqs. (15) require $k_y \ll \frac{2\pi}{\lambda} \cos \theta \times \min\left(1, \frac{\cot \theta}{2}\right)$.
- ²⁹R. Thom, *Structural Stability and Morphogenesis* (Reading: Benjamin, 1975).
- ³⁰M. V. Berry, *Adv. Phys.* **25**, 1 (1976).
- ³¹M. McGuirk and C. K. Carniglia, *J. Opt. Soc. Am.* **67**, 103 (1977).
- ³²J. F. Myatt, R. K. Follett, J. G. Shaw, D. H. Edgell, D. H. Froula, I. V. Igumenshchev, and V. N. Goncharov, *Phys. Plasmas* **24**, 056308 (2017).
- ³³A. E. Siegman, *Lasers* (Mill Valley: University Science Books, 1986).
- ³⁴A. Colaitis, J. P. Palastro, R. K. Follett, I. V. Igumenshchev, and V. N. Goncharov, *Phys. Plasmas* **26**, 032301 (2019).
- ³⁵Y. I. Orlov and S. K. Tropkin, *Radiophys. Quantum Electron.* **23**, 979 (1980).
- ³⁶Y. A. Kravtsov and Y. I. Orlov, *Sov. Phys. Usp.* **26**, 1038 (1983).
- ³⁷C. Gomez-Reino, M. V. Perez, and C. Bao, *Gradient-Index Optics: Fundamentals and Applications* (Berlin: Springer, 2002).
- ³⁸K. Y. Bliokh and A. Aiello, *J. Opt.* **15**, 014001 (2013).
- ³⁹W. L. Kruer, *The Physics of Laser Plasma Interactions* (Boca Raton: CRC Press, 2003).
- ⁴⁰N. A. Lopez and F. M. Poli, *Plasma Phys. Control. Fusion* **60**, 065007 (2018).
- ⁴¹A. Colaitis, I. Igumenshchev, J. Mathiaud, and V. Goncharov, *J. Comput. Phys.* **442**, 110537 (2021).
- ⁴²N. A. Lopez and I. Y. Dodin, *New J. Phys.* **22**, 083078 (2020).
- ⁴³N. A. Lopez and I. Y. Dodin, *J. Opt.* **23**, 025601 (2021).
- ⁴⁴N. A. Lopez and I. Y. Dodin, *Phys. Plasmas* **29**, 052111 (2022).
- ⁴⁵Note that our notion of an aperture is different from that used in the detailed study of Ref. 56.
- ⁴⁶J. W. Goodman, *Introduction to Fourier Optics*, 3rd ed. (New York: Roberts, 2005).
- ⁴⁷M. Born and E. Wolf, *Principles of Optics*, 7th ed. (Cambridge: Cambridge University Press, 1999).
- ⁴⁸A. Colaitis, G. Duchateau, P. Nicolai, and V. Tikhonchuk, *Phys. Rev. E* **89**, 033101 (2014).
- ⁴⁹A. Colaitis, G. Duchateau, X. Ribeyre, and V. Tikhonchuk, *Phys. Rev. E* **91**, 013102 (2015).
- ⁵⁰A. Ruocco, G. Duchateau, V. Tikhonchuk, and S. Huller, *Plasma Phys. Control. Fusion* **61**, 115009 (2019).
- ⁵¹M. V. Berry and C. J. Howls, *Nonlinearity* **3**, 281 (1990).
- ⁵²E. R. Tracy, A. J. Brizard, A. S. Richardson, and A. N. Kaufman, *Ray Tracing and Beyond: Phase Space Methods in Plasma Wave Theory* (Cambridge: Cambridge University Press, 2014).
- ⁵³J. F. Nye, *Natural Focusing and Fine Structure of Light* (Bristol: IOP Publishing, 1999).
- ⁵⁴O. Vallee, M. Soares, and C. de Izarra, *Z. angew. Math. Phys.* **48**, 156 (1997).
- ⁵⁵J. Heading, *An Introduction to Phase-Integral Methods* (London: Methuen, 1962).
- ⁵⁶J. F. Nye, *J. Opt. A: Pure Appl. Opt.* **8**, 304 (2006).